Toughening and strengthening of visible light-cured hydroxyapatite thiol-ene resin composite intended as bone fixation using 2D textile

Guillaume Patt-Lafitte, Olivier Valfort, Daniel J. Hutchinson, Michael Malkoch, David Eglin

Journal of Materials Research and Technology 29 (2024) 982–990

Contents lists available at ScienceDirect

Journal of Materials Research and Technology

journal homepage: www.elsevier.com/locate/jmrt

Toughening and strengthening of visible light-cured hydroxyapatite thiol-ene resin composite intended as bone fixation using 2D textile

Guillaume Patt-Lafitte [a], Olivier Valfort [b], Daniel J. Hutchinson [c], Michael Malkoch [c], David Eglin [a,*]

[a] Mines Saint-Etienne, Univ Jean Monnet, INSERM, UMR 1059 Sainbiose, 42023, Saint-Etienne, France
[b] Mines Saint-Etienne, Univ Lyon, CNRS, UMR 5307 LGF, Centre SPIN, F-42023, Saint-Etienne, France
[c] Department of Fibre and Polymer Technology, KTH Royal Institute of Technology, Stockholm, SE 10044, Sweden

ARTICLE INFO

Handling editor: P.Y. Chen

ABSTRACT

Metals plates and screws are the gold standard in metacarpal and phalangeal fracture fixation as they provide high stability to complex fractures. However, incidence rates of complications ranging from 42 to 92 % have been reported. Bone bioadhesive fixation based on light-cured thiol-ene technology and reinforced with hydroxyapatite (HA) is a promising solution for customizable devices with tailored mechanical properties and reduced soft tissue adhesion. The reinforcement of these thiol-ene composites with 2D textiles or meshes has been proposed; however, their role in the mechanical performance has not been explored. In this study, structural and mechanical behavior properties of a light-cured resin composite with thiol-ene precursors and HA in the presence and absence of one and three-layer of poly(ethylene terephthalate) (PET) meshes were assessed. The lack of effect of the meshes on the light-cure efficiency and the structural homogeneity of the cured composite is shown using Raman spectroscopy, water uptake measurements, and micro-computed tomography. The insertion of meshes increased the strength and energy to fracture of resin-based composite. The woven geometry of the PET meshes enables frictional sliding behavior, and reduced crack propagation ensuring integrity after matrix failure. This effect increases with the number of meshes and was significantly higher in bending than in tensile stress conditions. Related to hand and wrist fractures, the design of composite fixation devices, based on HA and meshes fillers can significantly increase the strength and toughening of those medical devices with a potential impact on post-operation by reducing mechanical mismatch of stress shielding and prevent complications due to material disintegration, resulting from the compliant and personalized bone bioadhesive fixation application.

1. Introduction

Hand and wrist fractures represent almost 20 % of all fractures treated at emergency services [1,2]. Among those fractures, 59 % are phalangeal fractures, and 33 % are metacarpal fractures [1,3–5]. Most hand fractures can be treated conservatively, but some require surgery for reduction and stabilization. The gold standard for complex/unstable fracture is open surgery and fixation with metal devices such as plates, screws, and K-wires. Metal plates and screws are frequently employed as they provide higher stability and are less dependent on fracture type. Nonetheless, high complication rates, ranging from 42 % for plate fixation and up to 92 % in all cases have been reported [4–7]. This is partly attributed to the complex fractures treated, but also to issues associated with the fixation implant such as infections, finger stiffness, and stress shielding [1,4–9]. Tissue adhesions to metal plates commonly lead to finger stiffness and are caused by the invasiveness of the surgery, and the long-term impact of a foreign non-degradable surface and bulk material [10]. In this context, a fixation device that can be applied with less invasiveness and the absence of screws, where bone stock and quality may be insufficient would be relevant. Bone glues, which can either glue a device onto bone or directly stabilize bone fractures, are pertinent solutions [11,12]. Key challenges for the development of

Abbreviations: ORIF, Open Reduction Internal Fixation; HA, Hydroxyapatite; PET, Poly(ethylene terephthalate); PDMS, Polydimethylsiloxane; μCT, Micro-computed tomography; SEM, Scanning Electron Microscopy; CPC, Calcium Phosphate Cement.

* Corresponding author.
E-mail addresses: guillaume.lafitte@emse.fr (G. Patt-Lafitte), valfort@emse.fr (O. Valfort), danhut@kth.se (D.J. Hutchinson), malkoch@kth.se (M. Malkoch), david.eglin@emse.fr (D. Eglin).

https://doi.org/10.1016/j.jmrt.2024.01.127
Received 17 July 2023; Received in revised form 20 December 2023; Accepted 14 January 2024
Available online 17 January 2024

adhesive-based bone fixation are the need to develop concomitantly a strong bone material interface, while preventing soft tissue adhesions and installing relevant mechanical support for fracture stabilization with a highly biocompatible system.

An approach described by Granskog V. et al. [13], addresses these requirements through the combination of a primer formulation, to create adhesion of the fixation to bone, a mechanically competent light-cured material [13]. Emulating dental composite resins, the described device consists of a primer system, composed of molecules derived from 3-(allyloxy)-2-((allyloxy)-methyl)-2-methylpropanoic acid, which contains phosphonic acid and alkene pendant groups and thiol molecule from ethoxylated-trimethylolpropane tri-3-mercapto-propionate. The primer can bind to the bone but also interacts with a high-strength light-cured resin formulation constituted of trifunctional triazine–trione alkene, thiol monomers, and a light initiator [13]. The thiol-ene resin is cured through irradiation of a high-energy visible (HEV) light lamp and can be applied into the desired geometry for the creation of customized osteosynthesis fixation for low load-bearing bone, e.g. phalange and rib [14]. The thiol-ene light-curing achieves a high monomer conversion rate, resulting in less leaching of unreacted monomers, in addition to lower shrinkage upon curing, when compared to dimethacrylate-based resins [15,16]. Mechanical properties of light-cured thiol-ene formulations can be improved by the use of branched oligomers, but also by the inclusion of fillers such as dental glass or hydroxyapatite (HA) micro-particles [13,14,17]. For example, the addition of 56 w.w% of HA increased 3-fold the flexural modulus of the light-cured thiol-ene resin [13]. Poly(ethylene terephthalate) (PET) fiber meshes have also been included as reinforcement [13,14]. Although a large effort has been put into the optimization of the resin composite formulation in the absence of the PET meshes, the role and impact of the PET meshes on the curing, structural, and mechanical properties of the fixation device have not been fully explored [14]. An understanding of the effect of the meshes in conjunction with the particle filler is necessary for further improvement of the device's performance.

In this study, structural and mechanical properties of a light-cured resin composite with thiol-ene precursors and HA in the presence and absence of one and three PET meshes were assessed. More specifically, prepared fixation devices were characterized by Raman spectroscopy, three-point bending and tensile tests, scanning electron microscopy, micro-computed tomography, and water uptake analysis. The lack of effect of the meshes on the light-cure efficiency and the structural homogeneity of the cured composite are shown. An apparent reduction of voids is observed as well as a tendency toward higher maximum strength with an increased number of meshes. Toughening mechanisms as well as mode of failure leading to increased cohesion at high deformation are discussed in the context of the improvement of a bone fixation device.

2. Materials and methods

2.1. Fabrication of composites for mechanical, structural characterizations and Raman spectroscopy

Molds of 19 x 115 × 1 mm (l *x* w *x* t) and 2 mm thick for samples with 3 meshes (type IV specimen, ASTM D638-03), and molds of 6.5 x 33.5 × 2 mm were produced in PDMS (9:1, RTV615, Neyco, Vanves, France) and used for sample preparation [14]. The light curable resin composite was prepared by mixing 29.6 w:w% of tris[2-(3-mercapto-propionyloxy) ethyl]isocyanurate (Thiocure 331, 180 g mol^{-1} H active equivalent, Bruno Bock GmbH, Germany) with 14.0 w:w% of 1,3,5-triallyl-1,3,5-triazine-2,4,6(1H,3H,5H)-trione (TATATO, Sigma-Aldrich, St. Louis, MO, USA), 56.1 w:w% of hydroxyapatite (HA, reagent grade, Sigma-Aldrich, St. Louis, MO, USA; surface specific measured by N_2 sorption = 4.09 ± 0.01 m^2/g, agglomerate size measured by dry laser granulometry D10 = 0.225, D50 = 0.286 and D90 = 0.521 μm) and 0.25 w:w% of diphenyl(2,4,6-trimethylbenzoyl)phosphine oxide (TPO, Sigma-Aldrich, St. Louis, MO, USA). After 5 min of thorough mixing, the viscous uncured resin composite was left at rest for 60 min (for TPO powder homogenization) in the dark at room temperature. Then, the uncured resin composite was cast and cured using a polywave light-emitting diode (LED) lamp (Bluephase PowerCure, Ivoclar Vivadent AG, Schaan, Liechtenstein) with a wavelength range from 385 to 515 nm, an intensity of 2000 mW cm^{-2}, an illumination of 5 s per surface area and a distance of 1 mm to the exposed resin surface. The light-curing was performed on the exposed upper surface area, before removal of the sample from the PDMS mold and subsequent identical curing of the sample's lower surface (Fig. 1). The illumination time has been optimized previously and confirmed in this work for the resin composite showing no further reduction of the allyl peak intensity with increased light exposure [14].

Poly(ethylene terephthalate) (PET) meshes (PETWM757501, Polyester woven fabric, SurgicalMesh, CT, USA) were cut to the required mold shape in the warp and weft direction of the mesh using a laser cutter (Epilog Laser, Colorado, USA) at a 10 % power and 100 % speed setting. The PET mesh architecture was imaged and mechanically tested under uniaxial traction test (Supplementary data). The PET meshes were introduced in the resin composite after the laying of a first thin layer of uncured resin composite of circa 1 mm thickness. The meshes were positioned with the same fabric direction, either warp or weft, parallel to the long axis of the samples. The positioned mesh was then covered with uncured resin composite to fill up the mold or in sufficient quantity to cover the mesh prior to the addition of a second and third layer. Curing was performed after having made the entire patch first and then cured as described above. Prepared samples were stored in dry and dark conditions prior to analyses. Dog bone samples were solely used for the tensile test, while the beam samples were used for three-point bending, Raman spectroscopy, micro-computed tomography analysis, water absorption, and mass loss tests.

2.2. Mechanical tests

Uniaxial mechanical tests were performed on an Instron 3343 machine (Instron Corporation, Norwood, MA, USA) equipped with a 500 N load cell at a speed of 5 and 1 $mm.min^{-1}$ respectively for the tensile and three-point bending tests, with a lower contact of 30 mm for the bending test. Samples were tested at 25 °C and analyses stopped after sample failure or maximum displacement of 5 mm (occurrence of samples slippage). Five replicate measurements were performed for each test condition. The data were collected using the Bluehill Universal material testing software from Instron and exported to OriginPro 9.1. software (OriginLab corporation, Northampton, MA, USA) for analysis. The Young modulus was calculated as the slope of the stress-strain curve. The tensile strength was calculated following equation (1), where F_{max} is the maximum load, L is the displacement, A_0 is the initial area, and L_0 is the initial length. The flexural modulus value was calculated using equation (2), where l is the distance between the lower contacts, m is the slope of the load-displacement curve, w is the width of the beam, and d is the thickness of the beam. The flexural strength was calculated following equation (3), where l is the distance between the lower contacts, w is the width of the beam, d is the thickness of the beam, and F_{max} is the maximum load. The energy to failure was not accessible for all samples containing PET meshes (15 out of 19 samples unbroken) tested in three-point bending over a broad range of displacement of the moving crosshead (5 mm). Therefore, strain energy density (G) values were calculated for bending and tensile tests following equation (4), where A is the area under the load-displacement curve at different displacements and computed using the Peak Analyser function of OriginPro 9.1 software, w is the width of the beam and d is the thickness of the beam [18]. G_{resin} refers to the strain energy density at maximum stress ($\sigma_{t/f,max}$) of the resin composite response and G_{mesh} refers to the second strain energy density corresponding to the energy at maximum stress until maximum displacement (5 mm or break), G_{total} was calculated as $G_{resin} + G_{mesh}$.

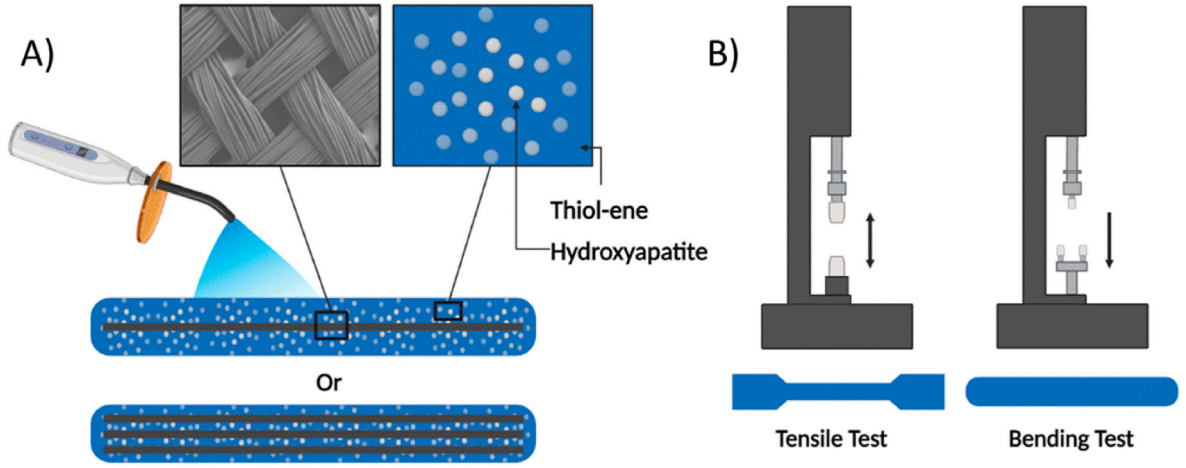

Fig. 1. Schematic overview of the photo-curable resin composite with the addition of 1 or 3 meshes and their mechanical test and shape.

The average values of the thickness and the width were calculated from caliper-recorded measurements at six locations lengthwise along each sample.

$$\sigma_{t,max} = \frac{F_{max}\, L}{A_0\, L_0} \tag{1}$$

$$E_f = \frac{l^3\, m}{4\, w\, d^3} \tag{2}$$

$$\sigma_{f,max} = \frac{3\, F_{max}\, l}{2\, w\, d^2} \tag{3}$$

$$G = \frac{A}{w\, d} \tag{4}$$

2.3. Raman spectroscopy

Raman spectroscopy was performed on a Micro Raman Confocal Xplora spectrometer (HORIBA Ltd., Jobin Yvon, France). Samples were scanned with a 532 nm laser source with a 10× working distance objective. The laser was projected onto a focal spot with a beam diameter of 1 μm. Spectra were acquired over 32 scans with a spectral resolution of 3.7 cm^{-1}.$pixel^{-1}$ over a spectral range of 1000 to 3200 cm^{-1}. Raman analysis was performed 5 times on the surface of the uncured resin composite (one sample) and one time on the surface of 5 independently cured samples. The spectra were collected, their baseline was automatically corrected using LabSpec software and normalized by the carbonyl vibration (1766 cm^{-1}) of each sample of the triazine-trione ring on the alkene and thiol monomers, the intensity of which is unaffected by the light-curing. Sample spectra were exported in Origin 9.1 software; the automatic peak analyzer function was used to measure the intensity value of the allyl and thiol vibrational signals at 1650 and 2584 cm^{-1} respectively. The estimated error values on the normalized peak were 5 % for allyl intensity and 8 % for thiol intensity for the uncured sample and 10 % for the cured samples with low peak intensity.

2.4. Micro-computed tomography (μCT)

Micro-computed Tomography (μCT) analysis was performed on a Nanotom 180 (GE Sensing & Inspection Technologies Phoenix X-ray, CA, USA) instrument. The specimens were scanned at a 100 kV voltage, a 60 μA intensity, and 500 ms integration times, with a 9.8 μm theoretical resolution. Two-dimensional CT images were scanned, the DICOM files were collected using VGStudioMax 2.0 and Avizo 9.0 software, and exported in cTAn software (Bruker microCT, MA, USA) for analysis. To evaluate voids within the samples, grey-value images were filtered with the condition mean function to have a grey-smooth image and converted to binary images through the threshold function. Structural indices were collected through the 3D analysis function [19]. Among them, the total porosity (P_{total}) was calculated using equation (5). The open porosity (P_{open}) was calculated using equation (6), where the volume of open pores corresponds to space located within a solid or between a solid, which has any connection in 3D to the space outside the object or objects. The close porosity (P_{close}) was calculated using equation (7), where the volume of close pores corresponds to black voxels fully surrounded by white voxels.

$$P_{total} = \frac{volume\ of\ close\ pores + volume\ of\ open\ pores}{total\ volume}\, x100 \tag{5}$$

$$P_{open} = \frac{volume\ of\ open\ pores}{total\ volume}\, x100 \tag{6}$$

$$P_{close} = \frac{volume\ of\ close\ pores}{binary\ ROI + volume\ of\ close\ pores}\, x100 \tag{7}$$

2.5. Scanning electron microscopy (SEM)

SEM images of three-point bending fractured samples were collected using a Zeiss SUPRA 55 VP instrument (Zeiss, Oberkochen, Germany). Specimens were fixed on double-sided carbon tape, the edge covered with silver lacquer, and metallized with gold at 20 mA during 50 s (Q150R, Quorum Technologies, UK). Observations were performed with the InLens mode at 2 kV and 5 and 10 mm WD.

2.6. Water absorption

The water absorption test consisted of the initial measurement of the sample's dry mass (M_1) using a microbalance (AdventurerPro, OHAUS Europe GmbH, Switzerland), and their following immersion in phosphate-buffered saline (PBS, 0.05 samples to PBS w/v ratio) at 37 °C. Samples were then collected, blotted with tissue, and weighed to give their wet mass (M_2) every two days during 2 weeks and re-immersed in PBS at 37 °C until constant values were reached. The samples were finally dried again to constant mass (M_3). The water absorption was calculated using equation (8) and the mass loss was calculated using equation (9).

$$Water\ absorption = \frac{M_2 - M_1}{M_1} x100 \tag{8}$$

$$Mass\ loss = \frac{M_1 - M_3}{M_1} x100 \tag{9}$$

2.7. Statistical analysis

Tensile, three-point bending, and Raman spectroscopy results were analyzed using OriginPro 9.1 software. After testing the distribution normality, one-way analysis of variance (ANOVA) post-hoc Tukey HSD tests were performed to compare groups (p-value <0.05).

3. Results

3.1. Effect of PET meshes inclusion on the curing efficiency of the resin composite

The Raman spectra of the resin composite prior to curing show vibrational peaks at 1645, 1759, and 2575 cm^{-1} respectively attributed to allyl, carbonyl, and thiol vibrations, are plotted on Fig. 2b. Upon light-curing the allyl and thiol chemical groups are reacted to form a thio-lether. This leads to the disappearance of the respective Raman vibrations while leaving the carbonyl peak unaffected as shown on Fig. 2A. After normalizing the allyl and thiol peaks by the carbonyl peak, it was found that the ratio between the normalized intensity of cured samples over the normalized intensity of the uncured samples was circa 12 %. Resulting in a conversion of more than 88 % of the allyl and thiol peaks. The introduction of PET mesh to the resin did not affect curing efficiency, as there was no significant difference in the normalized intensity values for all the cured groups tested (number of layers of mesh, orientation, and size of test samples). Similarly, Raman spectra collected along the test samples section indicated similar curing throughout indicating that the PET meshes do not prevent adequate curing for the prepared samples, even with a sample thickness of 2 mm.

The water absorption and mass loss of the samples on Table 1, were determined as 2 % and 0.1 % or less, respectively, for all the samples with and without PET mesh. This indicated a marginal water uptake and the absence of significant leachable products within the 14 days of the in vitro experiment. This points to a lack of influence of the introduction of the PET mesh onto the curing protocol effectiveness.

3.2. Effect of PET meshes inclusion on the structural properties of the resin composite

The resin composite is visible in the μCT images on Fig. 3A as an inhomogeneous light grey region with white micrometric regions corresponding to HA aggregates dispersed throughout. The PET meshes have a darker and more homogenous grey value (lower density) with fiber bundle organization visible. No gaps or regions with lower density are observed at the interface between the resin composite and the PET meshes at the resolution of 10 μm. Representative μCT images of the resin composite in the presence and the absence of PET meshes show spherical voids homogenously distributed within the resin composite. The spherical voids were likely air bubbles entrapped in the viscous uncured resin composite formulation during the mixing of the raw compounds and the fabrication of samples. According to the histogram of the voids on Fig. 3B, the spherical voids have an average size value of 100 μm, which does not change with the addition of meshes. This is supported by calculated values on Table 2, such as the degree of anisotropy found for the porosity, with values close to zero.

Table 1
List of water absorption and mass loss values. (n = 2).

Mesh layers	Water absorption [%]	Mass loss [%]
0	2 (0.1)	0.1 (0.1)
1	2 (0.1)	0.1 (0.1)
3	1.8 (0.2)	0.0 (0.0)

The open porosity significantly increases with the addition of meshes, from 5, 11 and 16 % (Table 2). The calculated open porosity matches in a good approximation the volumes of the meshes as the regions of interest for the μCT reconstruction were defined in order to have the meshes throughout the reconstruction volumes. Whereas close porosity significantly decreases with the addition of meshes, from 11, 8, and 4 % (Table 2). Which corresponds mainly to voids fully surrounded by material. This may explain the total porosity increase with the addition of meshes from 15, 18 and 19 %.

Representative high-magnification SEM images of the resin composite with three PET meshes fracture sites are shown in Fig. 4.

The images 4.A and 4.B show the PET filaments in bundles either intact, broken, or deformed after failure of the resin composite in a three-point bending test. Stretching scars on the filament's surface (Fig. 4C) indicate deformation of the filaments until breakage. Scratching scars and fragments of resin composite are also visible on the filaments surface showing slip-hardening and pullout effects. The

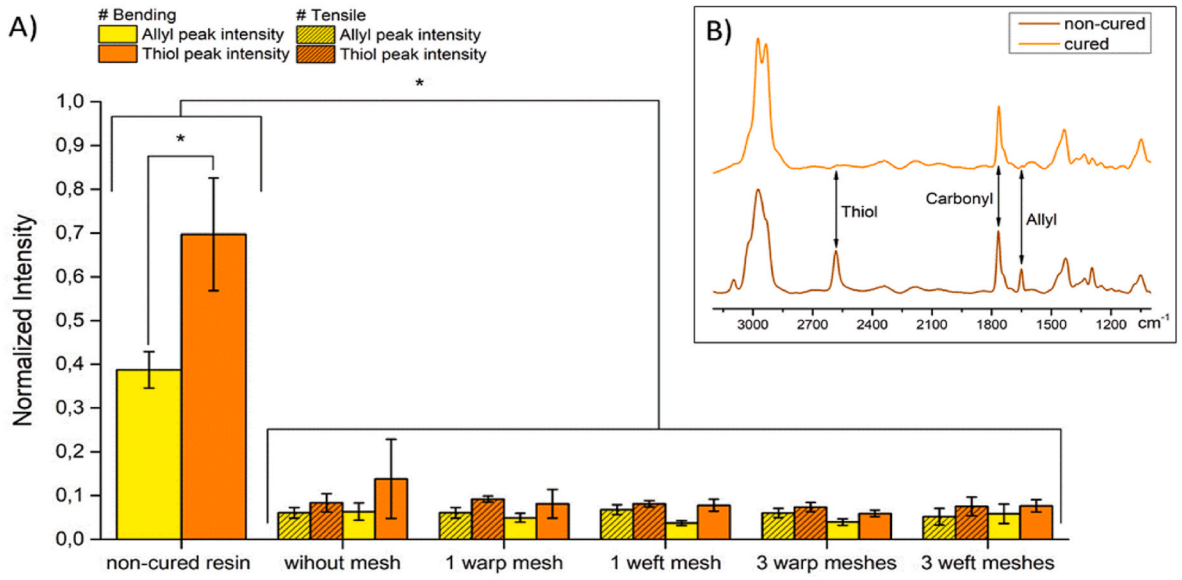

Fig. 2. (A) Plot of the allyl and thiol vibrational peaks intensity values for the uncured resin composite, cured resin composite without and with PET meshes (intensities after normalization to carbonyl vibrational peak with, in yellow ally-groups and in red thiol-groups for bending and tensile conditions, n = 5, p-value <0.05). (B) Representative Raman spectra of the non-cured (brown) and light-cured resin composite (orange).

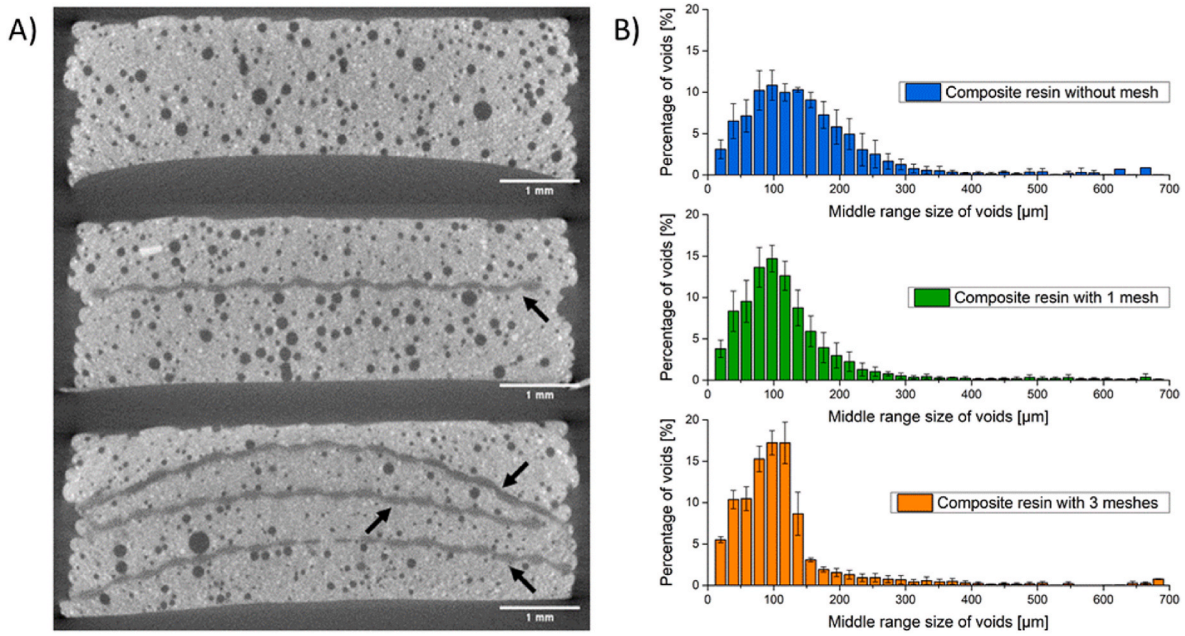

Fig. 3. Voids structure analysis in the resin composite without and with PET meshes. (A) Representative µCT images (mesh showed by black arrows). (B) Histogram of the size of the voids in function of their percentage in the material (n = 5).

Table 2
List of porosities values, degree of anisotropy, and range void size calculated from µCT data. Values are mean values of n = 5, with a standard error in brackets.

Mesh layers	Total porosity [%]	Open porosity [%]	Close porosity [%]	Degree of anisotropy	Range of major void size [µm]
0	15 (1)[a]	5 (1)[a]	11 (1)[a]	0.2 (0.03)[a]	107.4 ≤ - ≤ 126.9
1	18 (4)	11 (4)[a]	8 (1)[a]	0.3 (0.04)[a]	87.9 ≤ - ≤ 107.4
3	19 (1)[a]	16 (1)[a]	4 (1)[a]	0.3 (0.02)[a]	87.9 ≤ - ≤ 107.4

[a] correspond to p-value >0.05 for Total porosity, $_{I1\text{-}I3}$; Open porosity, $_{I1\text{-}I2}$; $_{I2\text{-}I3}$; $_{I1\text{-}I3}$; Close porosity, $_{I1\text{-}I2}$; $_{I2\text{-}I3}$; $_{I1\text{-}I3}$; Degree of anisotropy, $_{I2\text{–}I3}$; $_{I1\text{-}I3}$.

presence of resin composite fragments on the PET filaments observed by SEM correlates with the µCT observations, and suggests a good infiltration. On the images 4.D and 4.E, a rough fractured surface with the presence of meso-voids and HA particles surrounded by the resin is visible. The higher magnification image 4.F shows a HA particle negative topography imprinted on the fractured resin surface indicating pullout of some HA fillers that can be associated to a debonding mechanism [20].

3.3. Effect of PET meshes inclusion on the tensile and flexural properties of the resin composite

Representative flexural and tensile stress-strain curves of the resin composite without and with PET meshes are plotted in Fig. 5. List of moduli and strengths values are reported in Table 3.

The resin composite shows similar behavior in bending and tensile conditions with an initial linear stress-strain curve followed by a straight failure at an ultimate stress value ($\sigma_{f,max}$), also defined as the break strength values, at 1 % and 2 % strain respectively in bending and tension. The maximum strain or amount of deformation/deflection is higher in the tensile condition, 2 % than in the bending condition, 1 %. The flexural modulus value was 3 times higher than Young's modulus value: 5 (1) and 2 (1) GPa respectively (Table 3). The flexural strength value was 2 times higher than the tensile strength value: 43 (2) and 22 (2) MPa respectively. After the insertion of PET mesh in both testing conditions, frictional sliding phenomena were observed as a plateau with a significant load after the break strength value (post-breakage of the composite). The plateau load values increased with the number of PET meshes from 10 (3) to 35 (2) MPa for bending, and 9 to 14 (1) MPa for tensile. In this region, a relatively constant value of stress was measured for a long range of strain in bending, and a continuous decrease of the stress was observed in tensile. The strain to complete failure was drastically increased in bending condition, >4 % strain while it was increased by less than 1 % in the tensile condition. For the resin composite with one and three PET meshes, moduli values did not change significantly in comparison to the resin composite without mesh. There was a slight tendency for an increase in flexural moduli, flexural strength, and tensile strength when meshes were introduced in the warp direction compared to the weft direction. The ultimate strength value in the second region increased with the addition of PET meshes: 3.5 times higher in the bending condition and 1.7 times higher in the tensile condition.

The strain energy density G (or fracture energy) values shown in Fig. 6, correspond to the region of the resin composite (G_{resin}), the region of the PET meshes (G_{mesh}), and the total region (G_{total}), calculated for both testing conditions. The total strain energy density G values measured increased significantly with the addition of meshes in the bending condition while remaining constant in the tensile condition. The positioning of the PET meshes in the direction of the warp or weft did not significantly impact the G values. In both testing conditions, the values of the G_{resin} part (blue area) did not change with the addition of PET meshes. Whereas the values of the G_{mesh} part (green area) increased with the addition of PET meshes in bending condition and stayed constant in tensile condition. The increase in strain energy density corresponded to an increase in the toughening mechanisms of the resin composite when PET meshes were added. The energy gained was more significant in bending than in the tensile condition.

4. Discussion

Light-curable composite thiol-ene resin intended as a customized bone fixation device for complex phalange fractures has the potential to

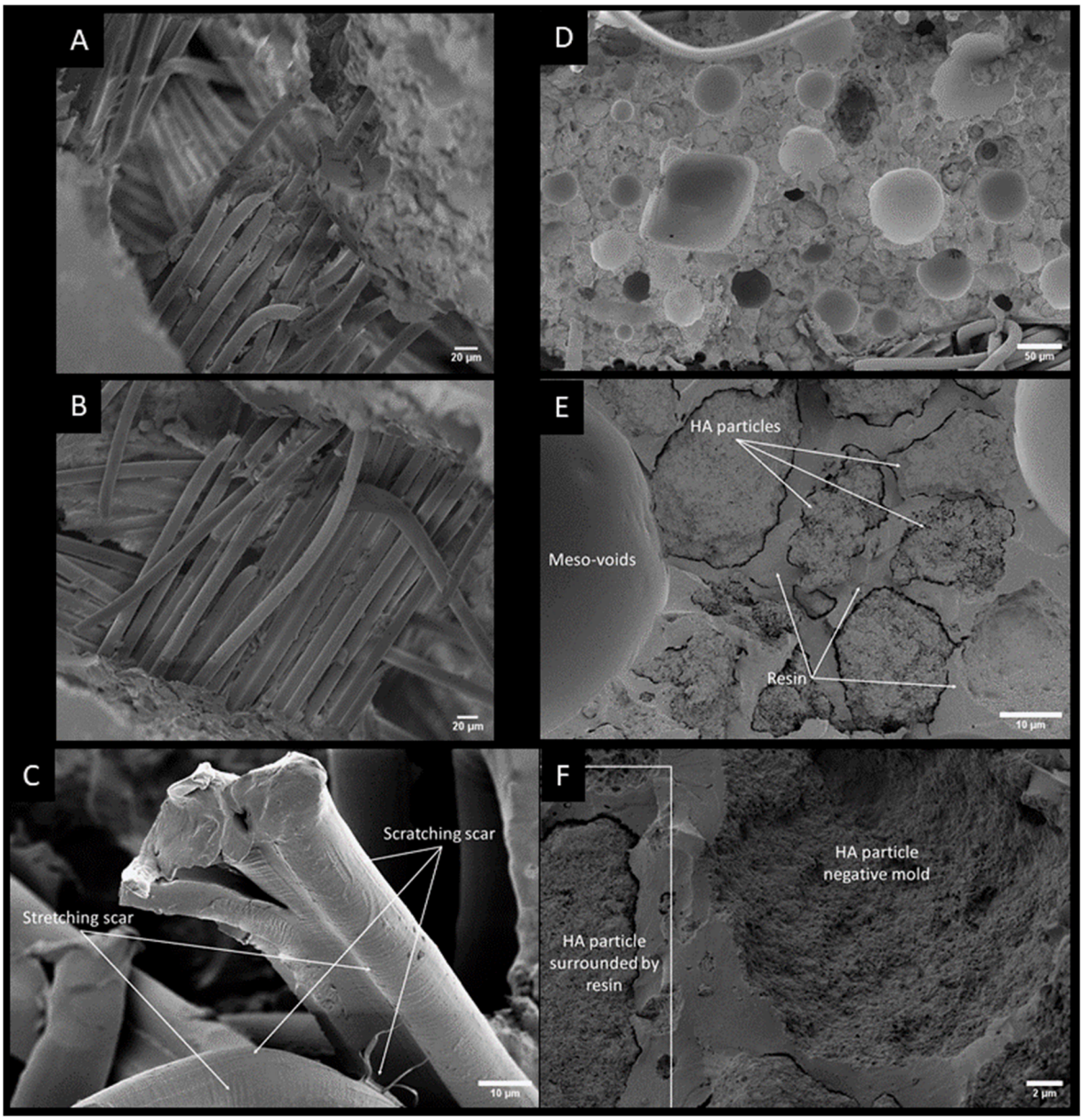

Fig. 4. Representative SEM images of the PET mesh (A–C) and the resin composite (D–F) on the fracture site of the resin composite sample with three meshes.

decrease complications through ease of customization and restoration of adequate mechanic property [9]. The light-cured thiol-ene resin containing HA filler has flexural modulus and strength values of 5 (1) GPa and 43 (2) MPa. These are close to previously reported results, two times higher than the light-cured thiol-ene resin without filler and four times lower than cortical bone [13,14,21]. The HA inorganic phase dispersed in the light-cured organic phase is responsible for significant reinforcement, reaching flexural strength comparable to values reported for calcium phosphate cements (CPCs) and other thiol-ene composites. Flexural moduli values ranging from 1.15 to 8 GPa and strength values ranging from 3.1 to 76 MPa have been reported for CPCs [22–26]. Flexural moduli values ranging from 1.6 to 10 GPa and flexural strength values ranging from 52 to 127 MPa have been reported for thiol-ene resin formulations loaded with 65 w.w% glass filler [17]. Inhomogeneity in the µCT images density values (Fig. 3) indicates HA-rich regions above 10 µm in size in the thiol-ene resin. Additionally, 11 % of porosity in the shape of spherical voids or meso-voids with a degree of anisotropy close to zero and size around 100 µm (Table 2, Fig. 3b) are attributed to entrapped air during formulation [27]. Not dissimilar to CPCs, the stress-strain curves of the resin composite displayed a rather brittle failure at 1 and 2 % strain in bending and tension (Fig. 5), corresponding to a low energy to failure material behavior which could lead to reduced fracture resistance against impact stresses (Fig. 6). The incorporation of a high amount of HA particles in a ductile thiol-ene resin has led to an embrittlement of the resulting composite.

Raman spectra showed a drastic reduction of the allyl and thiol peak vibration intensities to an identical level for all cured samples with and without meshes (Fig. 2). Water absorption and mass loss results (Table 1) indicated a minimal water uptake of 2 w.w%, and negligible weight losses for all samples. Thus, it can be inferred that similar curing is achieved in the presence or the absence of PET meshes. Remnants of allyl and thiol vibrational Raman signals after light-curing suggested an incomplete reaction of the stoichiometric formulation due to steric hindrance independent of the fillers load [28]. Complete disappearance of the allyl and residual thiol signal was observed by Trey S.M. et al., upon complete curing [29]. µCT images indicated a good impregnation of PET meshes at the microscopic level. Unexpectedly, the volume of close porosity calculated from µCT results and attributed mainly to

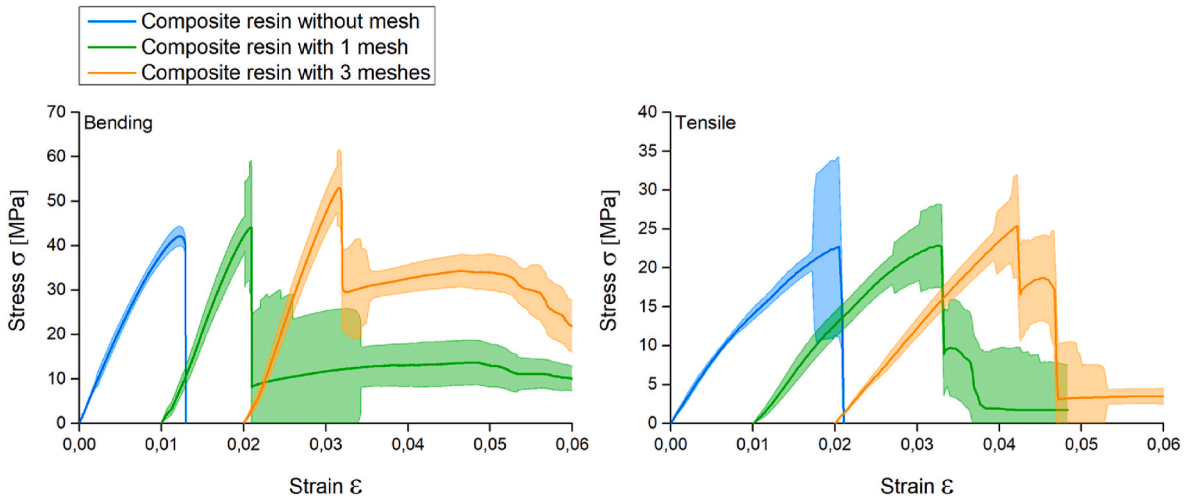

Fig. 5. Representative stress-strain curves of bending condition (left) and tensile condition (right) for resin composite without PET mesh (blue), with one PET mesh layer (green) and with three PET meshes (orange). Curve areas are the sample's standard deviation of the mean (curves are shifted to 0.01 in strain to better visibility).

Table 3
List of moduli and strengths in bending and tensile conditions of samples. Values are mean values of n ≥ 4, with standard error in brackets.

Mesh layers	Direction	Bending			Tension		
		E_f [GPa]	$\sigma_{f,G_{resin}}$ [MPa]	$\sigma_{f,G_{mesh}}$ [MPa]	E_t [GPa]	$\sigma_{t,G_{resin}}$ [MPa]	$\sigma_{t,G_{mesh}}$ [MPa]
0	–	5 (1)	43 (2)[a]	–	2 (1)	22 (2)	–
1	warp	5 (1)	47 (5)	13 (5)	2 (1)	20 (2)[a]	9 (4)
	weft	5 (1)	41 (5)[a]	8 (2)	2 (1)	18 (3)[a]	9 (2)
3	warp	5 (1)	50 (4)	37 (5)	2 (1)	24 (2)[a]	15 (6)
	weft	5 (1)	45 (4)[a]	34 (2)	2 (1)	21 (2)	13 (6)

[a] correspond to p-value >0.05 for $\sigma_{f,\ l1\text{-}l5}$; $\sigma_{f,\ l3\text{-}l5}$; $\sigma_{t,\ l2\text{-}l4}$; $\sigma_{t,\ l3\text{-}l4}$.

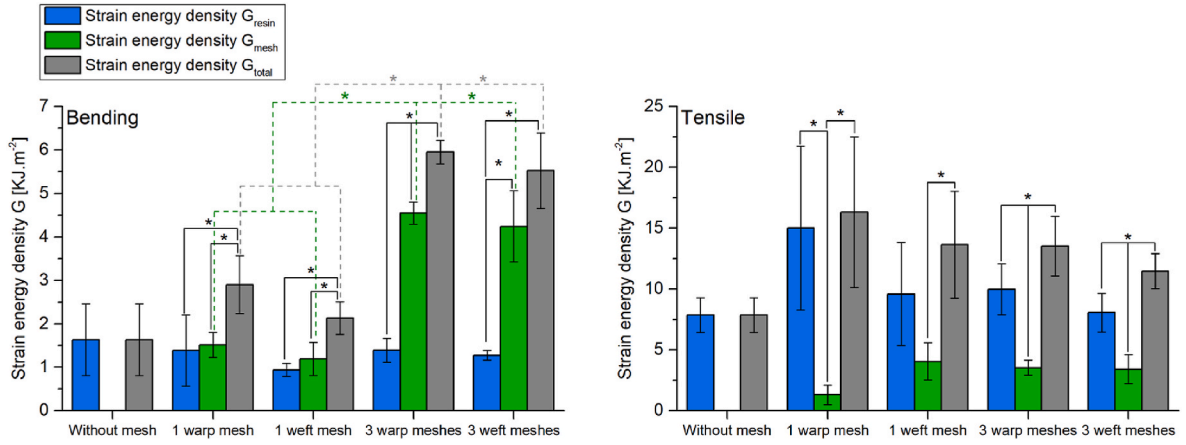

Fig. 6. Histogram plot of mean *G* values in bending condition (left) and in tensile condition (right), for the resin composite without and with PET meshes. Mean values (n ≥ 4) of the area under the load-displacement curves with, in blue the 1st part of the curves until the initial break, in green the 2nd part of the curve, and in grey the whole curve (see insert, P-value <0.05).

meso-voids content in the resin composite is reduced by 50 % with the inclusion of three meshes (Table 2). This slight reduction of entrapped air in the composite could be attributed to a capillarity effect upon impregnation of the meshes [30]. The reduction of meso-voids could likely improve the strength of the composite and reduce variability between samples [27]. However, competing mechanisms can affect the composite fracture's behavior such as reduced formation or faster propagation of cracks upon reduction of meso-voids. Thus, further experiments are warranted to assess the impact of meso-voids reduction.

Nonetheless, we can infer that the addition of PET meshes was not detrimental to the light-cured resin's composite moduli in bending and tensile and slightly improved the resin's strength (Table 3). This behavior is comparable to previous reports on fiber-reinforced CPCs, where modulus was unchanged by the addition of fibers, but flexural strength significantly increased [23,25]. The rather incremental strength value improvement may be attributed to the amount and type of fillers in the thiol-ene resin. The HA particles weight fraction of 56 w.w % with high interfacial surface area developed with the organic phase is preponderant in comparison to PET meshes corresponding to a weight fraction of around 4 to 9 w.w%. Additionally, the PET mesh is a woven

textile introduced in the HA/thiol-ene resin, whereas Kucko N. W. et al. [23], and Kirillova A. et al. [25], used around 2.5 to 16 w.w% single fiber randomly introduced in the CPCs matrix [23,25]. More dramatically, the addition of meshes improved the composite toughening mechanisms (total strain energy density values) 2 to 4 times in bending, with a positive correlation with increasing mesh number (Fig. 6, left). In tension, an increase in toughening mechanisms was observed without significant correlation with the mesh number (Fig. 6, right). In addition, SEM was used to image the surfaces of the resin-based composite containing meshes after mechanical testing. The observations point out a debonding fracture [20] and a slip-hardening behavior of the PET meshes coherent with the stress-strain profiles [31,32]. The later comportment is also aligned with the preservation of three-point bending tested samples cohesion and the observed intact filament bundles at the fracture site. Interfacial debonding and crack deflection, crack bridging and sliding, and pull-out are the likely entwined energy dissipating fracture mechanisms. This is consistent with a low surface contact and a lack of specific chemical interactions between the PET meshes and the resin composite matrix. The difference in toughening observed in bending and tension is possibly related to the difference in energy/stress transfer from the resin composite matrix to the mesh during frictional sliding at the interfaces. The slip-hardening behavior is likely related to a jamming effect induced by the woven conformation of meshes and good infiltration of the resin composite rather than meshes-resin composite matrix adhesion. A tendency to higher moduli, strength, and strain energy density values when tested in the warp direction is consistent with a more linear plan orientation of the PET fibers in comparison to weft (Figure B1 and A.1, Table B1 and A1).

Overall, the combination of a high HA payload and polymeric meshes in the thiol-ene resin matrix allows for concomitant improvement of strength and toughening mechanisms without affecting the highly efficient light-curing. This improvement could be even more significant on thiol-ene resin samples, pre-immerged in aqueous solutions mimicking the biological conditions, who had reduced mechanical properties [14]. Its use as customized fixation could reduce stress shielding related to the use of metal plates with high modulus (120 GPa) by having a modulus closer to bone (15–25 GPa) [9,21]. Secondly, the effect of meshes on the reduction of void and toughening can improve resistance to stress and prevent implant fragmentation upon failure. Further improvements are required to reach strength closer to bone tissue such as further reduction of meso-voids content and surface functionalization of polymeric meshes for a higher bonding interface with the organic reactants. A.

5. Conclusion

In this study, we demonstrated the advantages of reinforcing composite resin fixation devices by textile mesh. Woven PET meshes showed excellent impregnation at a macro and micro scale, without affecting the light-curing process, regardless of the number of meshes. The insertion of meshes increased the strength and energy to fracture of the medical device. Indeed, the woven geometry of the PET meshes enables frictional sliding behavior, and reduced crack propagation, resulting in load support after matrix failure. This effect increased with the number of meshes and was significantly higher in bending than in tensile stress conditions. Relative to hand and wrist fractures, the design of composite fixation devices, based on dual fillers can significantly contribute to increased strength and toughening of those medical devices with better mechanical mismatch and potentially less post-complication related to breaking material, resulting in a compliant and personalized bone bioadhesive fixation application.

CRediT authorship contribution statement

Guillaume Patt-Lafitte: Conceptualization, Methodology, Formal analysis, Investigation, Data curation, Writing–Original Draft. **Olivier Valfort:** Investigation, of the micro-computed tomography part. **Daniel J. Hutchinson:** Validation, Resources, Project administration. **Michael Malkoch:** Validation, Resources, Funding acquisition. **David Eglin:** Validation, Resources, Data curation, Writing–Original Draft, Visualization, Supervision, Funding acquisition, All authors contributed to Writing–Review & Editing.

Declaration of competing interest

The authors declare the following financial interests/personal relationships which may be considered as potential competing interests:

Michael Malkoch reports a relationship with Biomedical Bonding AB that includes: board membership.

8. Acknowledgments

The authors are thankful to Marilyne Mondon and Laetitia Veille for their technical assistance. Dr. Peter Varga from the AO Research Institute Davos and Dr. Christian Nai En Tierp-Wong from RegionH are acknowledged for their critical reading. This project has received funding from European Union's Horizon 2020 research and innovation programme under grant agreement No.952150 (BoneFix).

Appendix A. Supplementary data

Supplementary data to this article can be found online at https://doi.org/10.1016/j.jmrt.2024.01.127.

References

[1] Van Onselen EB, Karim RB, Hage JJ, Ritt MJ. Prevalence and distribution of hand fractures. J Hand Surg Br 2003;28:491–5. https://doi.org/10.1016/s0266-7681(03)00103-7.

[2] G., Ustun G, Kargalio F, Akduman B, Arslan R, Kara M, Gursoy K, Kocer U. Analysis of 1430 hand fractures and identifying the 'Red Flags' for cases requiring surgery. J Plast Reconstr Aesthetic Surg 2022;75:286–95. https://doi.org/10.1016/j.bjps.2021.06.011.

[3] Angermann P, Lohmann M. Injuries to the hand and wrist - a study of 50,272 injuries. J Hand Surg British Eur 1993;18b:642–4. https://doi.org/10.1016/0266-7681(93)90024-A.

[4] Brei-Thoma P, Vogelin E, Franz T. Plate fixation of extra-articular fractures of the proximal phalanx: do new implants cause less problems? Arch Orthop Trauma Surg 2015;135:439–45. https://doi.org/10.1007/s00402-015-2155-4.

[5] von Kieseritzky J, Nordstrom J, Arner M. Reoperations and postoperative complications after osteosynthesis of phalangeal fractures: a retrospective cohort study. J Plastic Surg Hand Surg 2017;51:458–62. https://doi.org/10.1080/2000656x.2017.1313261.

[6] Page SM, Stern PJ. Complications and range of motion following plate fixation of metacarpal and phalangeal fractures. J Hand Surg Am 1998;23a:827–32. https://doi.org/10.1016/S0363-5023(98)80157-3.

[7] Neumeister MW, Winters JN, Maduakolum E. Phalangeal and metacarpal fractures oft he hand: preventing stiffness. Plast Reconstr Surg Glob Open 2021;9:e3871. https://doi.org/10.1097/GOX.0000000000003871.

[8] Guerrero EM, Baumgartner RE, Federer AE, Mithani SK, Ruch DS, Richard MJ. Complications of low-profile plate fixation of phalanx fractures. Hand (N Y) 2019;16:248–52. https://doi.org/10.1177/1558944719855684.

[9] Al-Tamimi AA, Quental C, Folgado J, Peach C, Bartolo P. Stress analysis in a bone fractured fixed with topology-optimised plates. Biomech Model Mechanobiol 2020;19:693–9. https://doi.org/10.1007/s10237-019-01240-3.

[10] Richard RG. The relevance of implant surfaces in hand fracture fixation. Osteosynthesis in the Hand: current Concepts. FESSH Instruct Course 2008:20–30. https://doi.org/10.1159/000138577.

[11] Norton MR, Kay GW, Brown MC, Cochran DL. Bone glue -The final frontier for fracture repair and implantable device stabilization. Int J Adhesion Adhes 2020;102647. https://doi.org/10.1016/j.ijadhadh.2020.102647.

[12] Procter P, Hulsart-Billstrom G, Alves A, Pujari-Palmer M, Wenner D, Insley G, Engqvist H, Larsson S. Gluing living bone using a biomimetic bioadhesive: from initial cut to final healing. Front Bioeng Biotechnol 2021;9:728042. https://doi.org/10.3389/fbioe.2021.728042.

[13] Granskog V, Garcia-Gallego S, von Kieseritzky J, Rosendahl J, Stenlund P, Zhang YN, Petronis S, Lyven B, Arner M, Hakansson J, Malkoch M. High-performance thiol-ene composites unveil a new era of adhesives suited for bone repair. Adv Funct Mater 2018;28:1800372. https://doi.org/10.1002/adfm.201800372.

[14] Hutchinson DJ, Granskog V, von Kieseritzky J, Alfort H, Stenlund P, Zhang YN, Arner M, Hakansson J, Malkoch M. Highly customizable bone fracture fixation

through the marriage of composites and screws. Adv Funct Mater 2021;31(41): 2105187. https://doi.org/10.1002/adfm.202105187.
[15] Lu H, Carioscia JA, Stansbury JW, Bowman CN. Investigations of step-growth thiol-ene polymerizations for novel dental restoratives. Dent Mater 2005;21:1129–36. https://doi.org/10.1016/j.dental.2005.04.001.
[16] Carioscia JA, Lu H, Stanbury JW, Bowman CN. Thiol-ene oligomers as dental restorative materials. Dent Mater 2005;21:1137–43. https://doi.org/10.1016/j.dental.2005.04.002.
[17] Reinelt S, Tabatabai M, Moszner N, Fischer UK, Utterodt A, Ritter H. Synthesis and UVpolymerization of thiol-modified triazine-based monomers and oligomers for the use in thiol-ene-based dental composites. Macromol Chem Phys 2014;215(14): 1415–25. https://doi.org/10.1002/macp.201400174.
[18] Peroglio M, Gremillard L, Gauthier C, Chazeau L, Verrier S, Alini M, Chevalier J. Mechanical properties and cytocompatibility of poly (ε-caprolactone)-infiltrated biphasic calcium phosphate scaffolds with bimodal pore distribution. Acta Biomater 2010;6(11):4369–79. https://doi.org/10.1016/j.actbio.2010.05.022.
[19] Hildebrand T, Laib A, Muller R, Dequeker J, Ruegsegger P. Direct three-dimensional morphometric analysis of human cancellous bone: microstructural data from spine, femur, iliac crest, and calcaneus. J Bone Miner Res 1999;14(7): 1167–74. https://doi.org/10.1359/jbmr.1999.14.7.1167.
[20] Vaziri SH, Abadyan M, Nouri M, Omaraei IA, Sadredini Z, Ebrahimnia M. Investigation of the fracture mechanism and mechanical properties of polystyrene/silica nanocomposite in various silica contents. J Mater Sci 2011;46:5628–38. https://doi.org/10.1007/s10853-011-5513-9.
[21] Wan YZ, Wang YL, Cheng GX, Han KY. Three-dimensionally braided carbon fiber–epoxy composites, a new type of material for osteosynthesis devices. I. Mechanical properties and moisture absorption behaviour. J Appl Polym Sci 2002; 85:1031–9. https://doi.org/10.1002/app.10495.
[22] Paknahad A, Kucko NW, Leeuwenburgh SCG, Sluys LJ. Experimental and numerical analysis on bending and tensile failure behavior of calcium phosphate cements. J Mech Behav Biomed Mater 2020;107:1033565. https://doi.org/10.1016/j.jmbbm.2019.103565.
[23] Kucko NW, Schickert SD, Marques TS, Herber RP, Van den Beuken JJJP, Yi Z, Leeuwenburgh SCG. Tough and osteocompatible calcium phosphate cements reinforced with poly(vinyl alcohol) fibers. ACS Biomater Sci Eng 2019;5(5): 2491–505. https://doi.org/10.1021/acsbiomaterials.9b00226.
[24] Xu HHK, Zhao LA, Detamore MS, Takagi S, Chow LC. Umbilical cord stem cell seeding on fast-resorbable calcium phosphate bone cement. Tissue Eng 2010;16: 2743–53. https://doi.org/10.1089/ten.tea.2009.0757.
[25] Kirillova A, Nillissen O, Liu S, Kelly C, Gall K. Reinforcement and fatigue of a bioinspired mineral-organic bioresorbable bone adhesive. Adv Healthcare Mater 2021;10(2):2001058. https://doi.org/10.1002/adhm.202001058.
[26] Kruger R, Groll J. Fiber reinforced calcium phosphate cements - on the way to degradable load bearing bone substitutes? Biomaterials 2012;33:5887–900. https://doi.org/10.1016/j.biomaterials.2012.04.053.
[27] Mehdikhani M, Gorbatikh L, Verpoest I, Lomov SV. Voids in fiber-reinforced polymer composites: a review on their formation, characteristics, and effects on mechanical performance. J Compos Mater 2019;53:1579–669. https://doi.org/10.1177/0021998318772152.
[28] Lowe AB. Thiol-yne 'click'/coupling chemistry and recent applications in polymer and materials synthesis and modification. Polymer 2014;55:5517–49. https://doi.org/10.1016/j.polymer.2014.08.015.
[29] Trey SM, Gamstedt EK, Mäder E, Jönsson S, Johansson M. Glass fiber reinforced high glass transition temperature thiol-ene networks. Appl Sci Manufact 2011;42: 1800–8. https://doi.org/10.1016/j.compositesa.2011.08.003.
[30] Madra A, El Hajj N, Benzeggagh M. X-ray microtomography applications for quantitative and qualitative analysis of porosity in woven glass fiber reinforced thermoplastic. Compos Sci Technol 2014;95:50–8. https://doi.org/10.1016/j.compscitech:2014.02.009.
[31] Kucko NW, Petre DG, de Ruiter M, Herber RP, Leeuwenburgh SCG. Micro- and macromechanical characterization of the influence of surface-modification of poly (vinyl alcohol) fibers on the reinforcement of calcium phosphate cements. J Mech Behav Biomed Mater 2020;109:103776. https://doi.org/10.1016/j.jmbbm.2020.103776.
[32] Choi JI, Lee BY. Bonding properties of basalt fiber and strength reduction according to fiber orientation. Materials 2015;8(10):6719–27. https://doi.org/10.3390/ma8105335.